

The thermal stability of topologically close-packed phases in the single-crystal Ni-base superalloy ERBO/1

**I. Lopez-Galilea, J. Koßmann,
A. Kostka, R. Drautz, L. Mujica
Roncery, T. Hammerschmidt, S. Huth &
W. Theisen**

Journal of Materials Science

Full Set - Includes 'Journal of Materials
Science Letters'

ISSN 0022-2461

J Mater Sci

DOI 10.1007/s10853-015-9579-7



Your article is protected by copyright and all rights are held exclusively by Springer Science +Business Media New York. This e-offprint is for personal use only and shall not be self-archived in electronic repositories. If you wish to self-archive your article, please use the accepted manuscript version for posting on your own website. You may further deposit the accepted manuscript version in any repository, provided it is only made publicly available 12 months after official publication or later and provided acknowledgement is given to the original source of publication and a link is inserted to the published article on Springer's website. The link must be accompanied by the following text: "The final publication is available at link.springer.com".

The thermal stability of topologically close-packed phases in the single-crystal Ni-base superalloy ERBO/1

I. Lopez-Galilea¹ · J. Koßmann² · A. Kostka^{1,3} · R. Drautz² · L. Mujica Roncery¹ · T. Hammerschmidt² · S. Huth¹ · W. Theisen¹

Received: 10 August 2015 / Accepted: 8 November 2015
© Springer Science+Business Media New York 2015

Abstract In Ni-base superalloys, the addition of refractory elements such as Cr, Mo, Co, W, and Re is necessary to increase the creep resistance. Nevertheless, these elements induce the formation of different kinds of intermetallic phases, namely, the topologically close-packed (TCP) phases. This work focuses on intermetallic phases present in the second-generation single-crystal (SX) Ni-base superalloy ERBO/1. In the as-cast condition, the typical γ/γ' structure is accompanied by undesirable intermetallic phases located in the interdendritic regions. The nature of these precipitates as well as their thermal stability between 800 and 1200 °C has been investigated by isothermal heat treatments. The investigation techniques include DSC, SEM, EDX, and TEM. The experimental information is complemented by (1) comparison with a structure map to link the local chemical composition with phase stability, as well as (2) thermodynamic calculations based on the CALPHAD method to determine the occurrence and composition of phases during solidification and in equilibrium conditions. The TCP phases Laves, μ and σ were identified in various temperature/time ranges.

Introduction

Ni-base superalloys are used for gas turbine blades that can operate at temperatures above 1000 °C. They are produced by combining vacuum induction melting with a Bridgman type of solidification process and require subsequent multiple step heat treatments that ensure the demanded microstructure [1–3]. A modified Bridgman process with a grain selector is used to exploit dendritic solidification to produce single crystals (SX) [4–10]. Their high-temperature strength is achieved through many years of microstructure and chemical composition optimization [9, 11, 12]. First-generation single-crystal superalloys contain γ' forming elements like: Al, Ti, and Ta. In the second generation, their high-temperature strength was significantly enhanced by addition of refractory elements, most importantly 3 wt% of Re. The content of Re was further increased up to 6 wt% in the third generation [13–17]. The high concentration of refractory elements, however, induces the formation of topologically close-packed (TCP) phases during casting or exposure to conditions of high temperature and stress [18]. Solidification causes segregation of the alloying elements between dendrite cores and interdendritic areas. This kind of segregation has harmful effects on the microstructure and mechanical properties of the material due to the non-uniform distribution of γ' precipitates and the formation of TCP phases in the interdendritic regions [13–16, 19, 20]. Common TCP phases are P (orthorhombic), R (rhombohedral), μ (rhombohedral), σ (tetragonal), and the Laves C14, C36 (both hexagonal), and C15 (cubic) [21]. They are typically composed of Ni, Cr, Mo, Co, W, and Re, which are elements effective against creep [9]. Further development of single-crystal superalloys results in a fourth generation, which is characterized by the addition of Ru to retard the precipitation of TCP's [11, 20].

✉ A. Kostka
aleksander.kostka@rub.de

¹ Lehrstuhl Werkstofftechnik, Ruhr-Universität Bochum, 44780 Bochum, Germany

² ICAMS, Ruhr-Universität Bochum, Bochum, Germany

³ Max-Planck-Institut für Eisenforschung GmbH, Düsseldorf, Germany

Specifically, ERBO/1 is a CMSX-4 type second generation of single-crystal superalloys. It has about 1 at.% Re to prevent and retard the γ' coarsening via its segregation to the γ/γ' interface [22], 2 at.% W, and 0.4 at.% Mo for solid solution strengthening. The precipitation of TCP phases is unwanted because of the reduction of the γ/γ' -hardening effect and the depletion of strengtheners in the γ -matrix [23–27]. Moreover, the precipitation of TCPs at high temperatures is frequently associated with the formation of voids that may potentially act as fracture initiation sites. Until now, the precipitation of TCP phases during the lifetime of single-crystal components and their mechanism is not fully understood. A better understanding of the formation of TCP phases is of great importance for the development of new single-crystal Ni-based superalloys.

This work focuses on the characterization of the intermetallic phases forming in the interdendritic regions of the as-cast Ni-base single-crystal superalloy ERBO/1 during solidification and their structural stability during heat treatment. Special emphasis is put on the correlation of the experimental data, namely, chemical compositions of the microstructural constituents with the theoretical approaches. A recently derived structure map [27] that has been designed to study TCP phases is applied. Making use of the experimentally observed local chemical compositions, the structure map allows anticipating the precipitation of intermetallic phases that are verified with electron diffraction (TEM) analyses. These results are compared with thermodynamic solidification calculations using the Scheil–Gulliver approximation and with equilibrium calculations.

Material and methodology

Material and heat treatments

The second-generation single-crystal Ni-base superalloy ERBO/1 provided by Doncasters Precision Casting, Bochum (Germany) is studied in the present work. The chemical composition of ERBO/1 is listed in Table 1 and it is similar to the well-known chemical composition of CMSX-4.

After a thorough analysis of the as-cast material, isothermal heat treatments were carried out at different temperatures, 800, 900, 1000, 1100, and 1200 °C, with

annealing times of 2, 4, 8, 16, 32, and 50 h, in order to study the stability of the intermetallic phases. Heat treatments were performed in a laboratory furnace in an inert argon gas atmosphere at atmospheric pressure followed by water quenching.

Microstructural characterization

Samples for scanning electron microscopy (SEM) analyses were cut perpendicular to the [001]-direction, mounted in epoxy, mechanically polished to mirror finish, and etched (etching solution: 40 ml H₂O, 20 ml HCl, 10 ml H₂O₂). The microstructures were investigated using an SEM Zeiss (LEO) 1530 VP at 8.5 mm working distance and 20 kV acceleration voltage for a secondary electron micrograph (SE) as well as for a backscattered electron (BSE) signal. Jeol JEM-2200FS transmission electron microscope (TEM) operated at 200 kV and equipped with STEM high-angle annular dark field (HAADF) detector and EDAX EDX system was applied for phase identification in as-cast material and after annealing for 1000 °C for 32 h. TEM specimens were prepared from regions of interest along the matrix/TCP interface using a Jeol JEM-9320 focused ion beam system (FIB) at 30 kV.

Calorimetry

The phase transition temperatures of the as-cast material were examined by differential scanning calorimetry (DSC) performed on a LINSEIS instrument using specimens of about 100 mg. The specimens were heated at 10 °C/min under a flowing helium atmosphere to a temperature of 1450 °C. Reaction temperatures were determined from heating curves by the tangent method [28].

Thermodynamic calculations

The CALPHAD method [29, 30], by means of the commercial software Thermo-CalcTM [31] version s and database TTNi7 [32], was used to predict the stability, volume fraction, and composition of phases in ERBO/1. Calculations were performed for in equilibrium conditions and Scheil–Gulliver solidification, which describes solute redistribution during solidification and considers infinitely fast diffusion in the liquid phase.

Table 1 Nominal composition of ERBO/1 in at.%. The corresponding structure map coordinates (\bar{N} , $\Delta V/\bar{V}$) according to Eqs. 1 and 2 are shown in the last two columns

	Alloying elements; content (at.%)										Structure map	
	Ni	Co	Cr	W	Re	Al	Ti	Ta	Mo	Hf	\bar{N}	$\Delta V/\bar{V}$
ERBO/1	63.0	10.0	7.5	2.1	1.0	12.6	1.3	2.2	0.4	0.03	9.15	0.139

Structure map

The structure map anticipates the crystal structure of a compound system from atomic properties of the constituent elements. The structure map employed in this work has been recently derived for TCP phases [26]. It uses the average valence band-filling

$$\bar{N} = \sum_i c_i N_i \quad (1)$$

and a composition-dependent relative volume difference

$$\frac{\Delta V}{\bar{V}} = \sum_{ij} c_i c_j \frac{|V_i - V_j|}{\frac{1}{2}(V_i + V_j)} \quad (2)$$

as structure map coordinates for a given compound composition. Here, c_i is the molar fraction, N_i the effective number of valence electrons, and V_i the atomic volume (computed from the metallic radii) of the alloying element i . The location within the structure map relative to distinct regions of TCP phase stability allows one to anticipate which TCP phases might precipitate for the given composition. The predictions of the structure map are also in line with state-of-the-art density functional theory (DFT) calculations as shown for various binary systems [33, 34]. The application of the structure map to a system with non-homogeneous distribution of elements (like a superalloy) requires the knowledge of the local chemical composition. In this work, we obtain this information by experiment (“[Microstructural characterization](#)” section) and by solidification modeling (“[Thermodynamic calculations](#)” section).

Results

Thermodynamic calculations: solidification

During solidification, a considerable segregation of alloying elements takes place and is responsible for heterogeneities and precipitation of TCP phases. The segregation behavior in ERBO/1 during solidification was estimated by the CALPHAD method using the TTNi7 database in equilibrium conditions and with the Scheil–Gulliver method for solidification, which considers infinitely fast diffusion in the liquid phase and no diffusion in the solid phase and therefore a solidification profile, including TCP phases, similar to that experimentally observed can be calculated. Figure 1a, b shows the solidification path of ERBO/1 according to the Scheil–Gulliver method. The first and dominating phase that forms is the γ -phase. The γ' -phase starts to form at 1295 °C. The maximum γ' -phase fraction is obtained at the end of the solidification, with a value of about 5.3 vol%. Small, but considerable amounts of the intermetallic phases B2, σ , and Laves are predicted at lower temperatures. The

calculated solidus (T_{sol}), liquidus (T_{liq}), and precipitation (T_{prec}) temperatures of intermetallic phases are listed in Table 2, together with the measured calorimetric values. Due to the low amount of intermetallic precipitates contained in as-cast ERBO/1, the solvus temperatures for the different precipitates could not be detected.

The element concentration in the liquid during solidification is depicted in Fig. 1c, d. Taking into account a dendritic solidification, it predicts the enrichment of Ta, Hf, and Mo in the interdendritic region, and a slight enrichment of Ti and Cr in the dendrite core. The calculated relative high local concentration of the early transition metals Ta, Hf, and Mo in the remaining liquid is responsible for the precipitation of intermetallic phases. This is also reflected in the structure map in Fig. 2a due to the larger metallic radii and lower band-filling of these atoms.

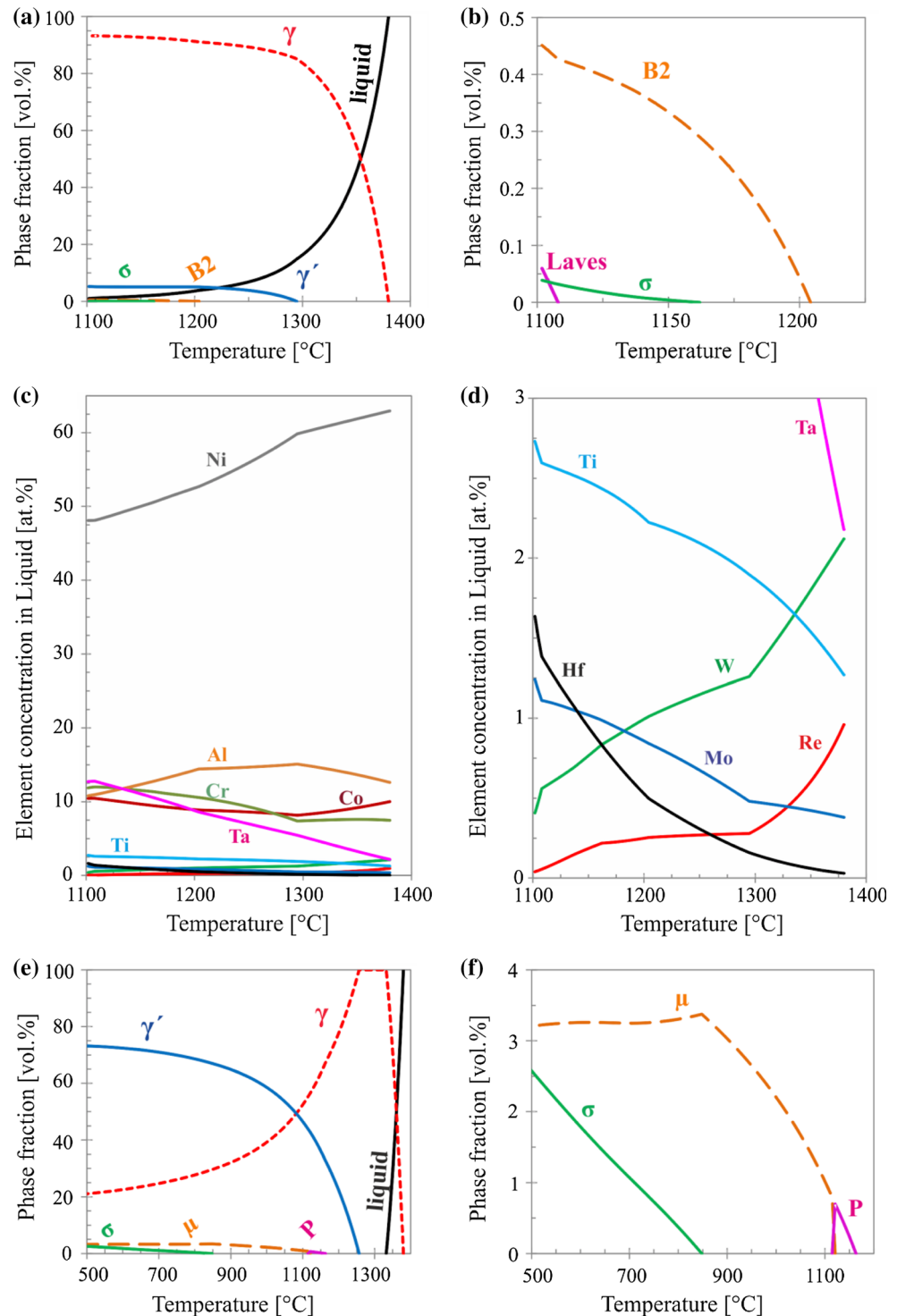
The calculated chemical composition of the minor intermetallic phases at the end of the solidification (1104 °C) is listed in Table 3. The B2-phase shows as main elements Ni, Al, and Ta. The σ -phase contains high concentrations of Cr, Co, and Mo and lower but substantial quantities of Re and W. Finally, the Laves-phase is characterized by high contents of Ta and Cr.

Thermodynamic calculations: equilibrium state

The phase composition and volume fraction of ERBO/1 in equilibrium as a function of the temperature was also considered. In contrast to the Scheil solidification, the first and single phase that forms during equilibrium solidification is the γ -phase (Fig. 1e, f). At a temperature of 1257 °C, the γ' -phase forms through solid-state transformation followed by the formation of the P -, μ -, and σ -phases, at 1163, 1121, and 848 °C, respectively. The amount of these minor intermetallic precipitates is not negligible and rises to 3.2 vol% for the μ -phase or 2.5 vol% for the σ -phase at 500 °C. The P -phase seems to be only stable in a narrow temperature range between 1164 and 1114 °C. The main transformation temperatures obtained for this calculation are listed in Table 2.

The chemical composition of the minor intermetallic phases predicted at equilibrium conditions is summarized in Table 4. As the P -phase is only stable in a narrow temperature range, its chemical composition is listed at 1121 °C. For the case of μ - and σ -phases, the compositions are shown at 600 °C. The chemical composition of the P -phase is very similar to that of the μ -phase. This is also in line with the structure map where the stability regions of the μ - and the P -phase overlap [27]. This observation, together with the fact that the amount of P -phase decreases with increasing μ -phase volume, suggests that the P -phase transforms into the μ -phase at approximately the same chemical composition. The main elements in the μ -phase are Co, Cr, W, Re, and Mo. The main elements in the σ -phase are Cr and Re.

Fig. 1 Thermodynamic calculations of the alloy ERBO/1 using the database TTNi7 (ThermoCalc). **a** Phase fraction during solidification using the Scheil–Gulliver approach. **b** Detail of Figure **a** in the range below 0.5 vol%. **c** Element concentration in the liquid phase during solidification estimated with the Scheil–Gulliver approach. **d** Detail of Figure **c** in the range below 3 at.%. **e** Equilibrium phase fraction. **f** Detail of Figure **e** in the range below 4 vol%



The phase fractions of the different phases predicted under equilibrium conditions at 800, 900, 1000, 1100, and 1200 °C are listed in Table 5. These temperatures correspond to the solution annealing temperatures in our experiments. We conclude that no other phase than γ and γ' is expected at temperatures above approximately 1200 °C.

Structure map and thermodynamic calculations

For each chemical composition of the different liquid and solid phases estimated from the thermodynamic calculations (cf. “Thermodynamic calculations: equilibrium state” section), we also computed the values of \bar{N} and $\Delta V/\bar{V}$ of

Table 2 Phase transformation temperatures (T_{liquidus} , T_{solidus} , and T_{solvus}) for ERBO/1 obtained experimentally from the DSC measurement of the as-cast materials as well as calculated using the

CALPHAD method and the TTNi7 database according to the Equilibrium and Scheil–Gulliver methods

Method	T_{liq} (°C)	T_{sol} (°C)	T_{solvus} (°C)					
			γ'	σ	μ	P	Laves	B2
DSC	1380	1320	–	–	–	–	–	–
Equilibrium	1379.8	1332.0	1256.7	848.1	1120.7	1163.3	–	–
Scheil	1379.8	1101.8*	1294.7	1162.0	–	–	1108.0	1204.1

* Scheil calculated T_{sol} with $\sim 1\%$ of liquid

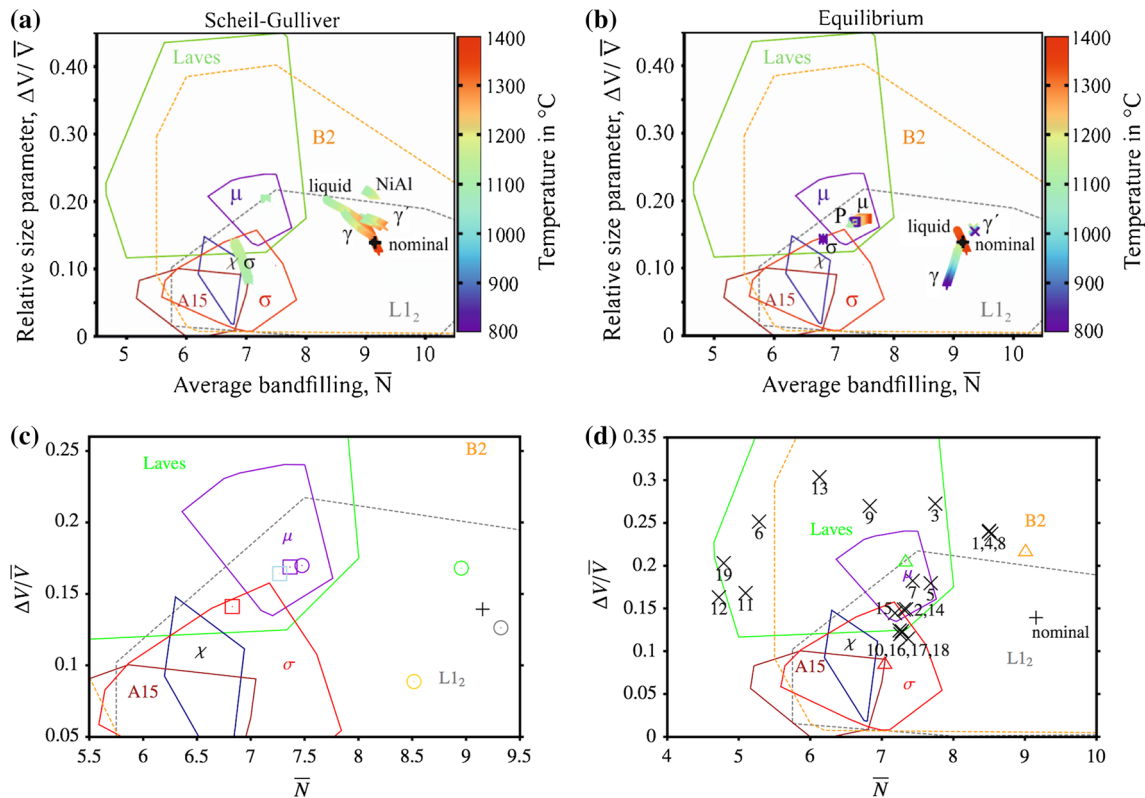


Fig. 2 Calculated structure maps revealing compositions of different phases present in ERBO/1. During solidification: **a** using the Scheil–Gulliver equation (shown in Fig. 1c, d), **b** Using the equilibrium phase fractions (shown in Fig. 1e, f). **c** After casting and **d** after heat treatment. Triangles indicate calculated compositions in the

solidification Scheil–Gulliver approach (Table 3). Squares indicate calculated compositions in equilibrium conditions (Table 4). Circles refer to element concentrations measured by TEM-EDX on as solidified samples (see Table 6). Crosses indicate measured compositions in heat-treated samples (Table 7)

the structure map (cf. “Structure map” section) according to Eqs. 1 and 2. The locations of the different phases in the structure map during solidification are represented in Fig. 2a, b as a function of temperature. The predicted phases according to the Scheil solidification are the B2, Laves, and σ -phase. Their chemical compositions are in agreement with the corresponding stability regions in the structure map (Fig. 2a). The predicted phases in equilibrium, μ and σ also are in agreement with the corresponding stability regions in the structure map (Fig. 2b). The P-phase stability region is not

shown in the structure map because it is known only for a very small region at about (7.6/0.170), see Refs. [27] and [35] for more details. However, this approximate position in the structure map is in good agreement with the predicted P-phase composition. The composition change of the remaining liquid during Scheil–Gulliver solidification (Fig. 1c, d) tends to elements with lower band-filling and higher volume factor, which leads the system towards the region of the TCP phase stability (Fig. 2a). This is also noticeable but less pronounced in the equilibrium solidification (Fig. 2b).

Table 3 Calculated chemical composition of B2, σ and Laves phases at 1104 °C according to Scheil–Gulliver calculations

	Fraction of alloying element (at.%)										Structure map	
	Ni	Co	Cr	W	Re	Al	Ti	Ta	Mo	Hf	\bar{N}	$\Delta V/\bar{V}$
B2	50.4	4.9	1.7	~0	~0	32.2	1.2	9.4	0.1	0.1	9.01	0.216
σ	11.0	18.6	59.1	2.6	2.8	0.5	0	0	5.4	0	7.04	0.084
Laves	28.9	14.9	26.1	3.1	0.1	0	0.9	25.5	0.5	~0	7.33	0.204

The corresponding structure map coordinates (\bar{N} , $\Delta V/\bar{V}$) according to Eqs. 1 and 2 are shown in the last two columns

Table 4 Calculated chemical composition of the P -phase at 1121 °C and the μ - and σ -phases at 800 °C according to equilibrium calculations

Phase	Fraction of alloying element (at.%)										Structure map	
	Ni	Co	Cr	W	Re	Al	Ti	Ta	Mo	Hf	\bar{N}	$\Delta V/\bar{V}$
P (1121 °C)	16.6	11.6	18.1	24.6	25.7	0	0	0	3.4	0	7.27	0.164
μ (800 °C)	16.4	16.8	15.2	25.6	20.5	0	0	~0	5.5	0	7.37	0.169
σ (800 °C)	7.1	9.5	41.8	13.5	25.9	~0	0	0	2.2	0	6.83	0.141

The corresponding structure map coordinates (\bar{N} , $\Delta V/\bar{V}$) according to Eqs. 1 and 2 are shown in the last two columns

Table 5 Calculated phase fractions of the different phases in equilibrium at 800, 900, 1000, 1100, and 1200 °C

Temperature (°C)	Phases; volume fraction (vol%)			
	γ	γ'	σ	μ
800	27.70	68.63	0.37	3.30
900	32.07	64.90	–	3.03
1000	39.23	58.57	–	2.20
1100	52.46	46.53	–	1.01
1200	77.69	22.31	–	–

The values are determined using the lever rule equation within the CALPHAD method and the TTNi7 database

Identification of intermetallic compounds in the as-cast state

The structure of the as-cast ERBO/1 reveals four-fold symmetric dendrites normal to the $\langle 001 \rangle$ growth direction without casting defects such as freckle chains. The primary dendrite arm spacing (PDA) for this material is between 400 and 500 μm [12]. The strong element segregation between dendrite core and interdendritic regions is responsible for heterogeneities and TCP phase precipitates. Previous work on segregation in ERBO/1 using electron probe microanalysis [12] demonstrates relatively high concentration of Al, Ti, Ta, Ni, and Hf in the interdendritic regions which rationalize the formation of intermetallic phases. The segregation of Cr, Co, W, and Re, in contrast, leads to high concentrations of these elements in the dendrite core. Figure 3 shows two micrographs of the as-cast ERBO/1 where two kinds of intermetallic precipitates are

visible. The intermetallic phases are present only in the interdendritic regions. TEM examination of this region confirmed the presence of the typical γ/γ' microstructure and showed two different particles adjacent to each other. The TEM selected area diffraction (SAD) patterns reveal that the brightest precipitate corresponds to the μ -phase and the darker to a Laves-phase. Chemical compositions obtained by EDX at the TEM of the characterized precipitates as well as of the γ and γ' -phases located at their side are compiled in Table 6. The respective \bar{N} and $\Delta V/\bar{V}$ values are depicted as circles in the structure map of Fig. 2c. The good agreement of experiment and structure map is apparent as the measured composition of the observed μ -phase (purple circle) is inside the corresponding stability region in the structure map. The position for the measured Laves-phase (green circle) is located in the structure map outside and to the right of its corresponding stability region, i.e., it is shifted to higher band-filling. Together with the results of our heat treatments (“[Structure map and thermodynamic calculations](#)” section) we suspect that some of the TCP precipitates are in fact metastable. The position of the interdendritic γ -matrix (yellow circle) is close to the σ -phase window, whereas the position of the interdendritic γ' -phase (gray circle) is inside its corresponding stability region.

The results of the TEM characterization of the as-cast ERBO/1 microstructure significantly differ from the solidification calculations. Comparing the values of the chemical composition shown in Tables 3 and 6, it is clear that our thermodynamic solidification calculations predict another kind of intermetallic phase and different chemical compositions. The experimental results as well as the Scheil–Gulliver calculations agree in the prediction of the

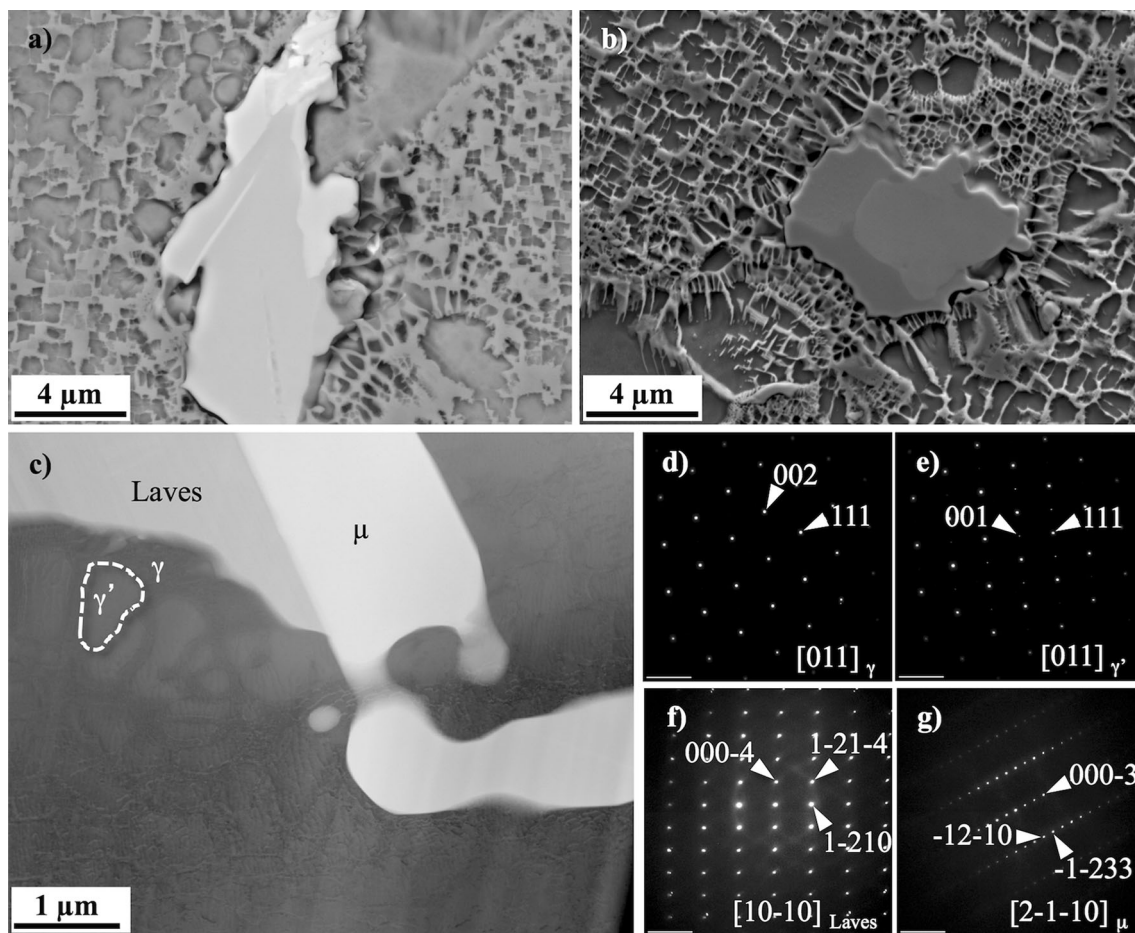


Fig. 3 Microstructural analyses of the as-cast ERBO/1. Intermetallic phases precipitated in interdendritic regions as observed by SEM **a** BSE detector and **b** SE detector. **c** STEM HAADF micrograph of

the interfacial region between μ and Laves-phase; **d–g** characteristic selected area diffraction patterns (SAD) taken from the individual phases

Table 6 Measured chemical composition of alloying elements [in at.%] obtained via TEM/EDX analysis of TEM the as-cast ERBO/1 alloy

	Fraction of alloying element (at.%)										Structure map	
	Ni	Co	Cr	W	Re	Al	Ti	Ta	Mo	Hf	\bar{N}	$\Delta V/\bar{V}$
Laves	71.6	10.7	2.3	0	0	1.0	0.8	2.1	0.4	11.1	8.96	0.168
μ	22.6	17.7	26.0	12.5	8.5	0.4	0.3	3.6	8.0	0.5	7.48	0.170
γ	47.7	17.0	26.5	1.3	0.9	3.5	0.6	0.3	1.9	0.2	8.52	0.089
γ'	74.1	7.9	2.7	0.4	0	7.9	2.8	2.0	0.3	1.9	9.32	0.126

The corresponding structure map coordinates (\bar{N} , $\Delta V/\bar{V}$) according to Eqs. 1 and 2 are shown in the last two columns

Laves-phase. However, the experimentally observed μ -phase is not predicted by this method. The equilibrium calculation predicts the formation of the μ -phase at temperatures below 1121 °C. The Laves-phase observed in as-cast ERBO/1 contains high amounts of Ni and Hf while the Scheil calculation shows high amounts of Cr, Ta, and Co. The μ -phase observed in as-cast ERBO/1 exhibits high amounts of Cr, Co, W, Re, and Mo that agree with the

prediction of our equilibrium calculations. As-cast ERBO/1 shows no σ -phase, although both thermodynamic calculations predict this phase. In addition, the P-phase or B2-phase as predicted by the simulations was not found in the experiment. The chemical composition of the precipitates predicted by Scheil–Gulliver calculations (Table 3) are compared with the experimental results (Table 6) by means of the structure map in Fig. 3c.

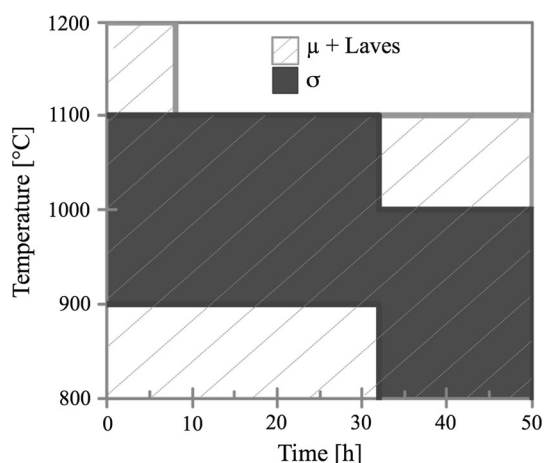


Fig. 4 Evolution of intermetallic precipitates in ERBO/1 after different heat treatments (temperatures range from 800 to 1200 °C and annealing times from 2 h to 50 h)

Thermal stability of intermetallic compounds

The applied heat treatments result in the dissolution of the precipitates in as-cast ERBO/1 and in the precipitation of new phases. Figure 4 summarizes the evolution of the intermetallic precipitates as a function of the heat treatment temperature and annealing time. Laves and μ -phase precipitates (line-pattern area) are observed during heat treatments at 800, 900, 1000, 1100 °C for the whole range of annealing times up to 50 h as well as at 1200 °C for annealing times up to 8 h. The total amount of Laves and μ -phase seems to be approximately constant during the heat treatments up to 900 °C and similar to the amount in the as-cast ERBO/1. The size and number of these precipitates decrease after annealing at temperatures above 1000 °C. Both, Laves and μ -phase detected in the as-cast state (Fig. 3) were also observed in the whole range of applied heat treatment. From our experiments, it is not clear if the particles dissolved independently or if they transform into one another.

For heat treatment at 800 °C with annealing times up to 16 h, we observe the two initial phases Laves and μ (Fig. 5a, b). Longer annealing times, however, lead to the additional precipitation of a needle-shaped phase at the interdendritic regions, identified as the σ -phase (gray solid area in Fig. 4). This phase is always present in the heat treatments at 900 or 1000 °C regardless of the annealing time. Figure 5c and d shows thin needles of the σ -phase after 4 h at 1000 °C. The number and size of these needle-shaped precipitates increases with increasing annealing time, adopting a Widmanstätten structure [25] as can be observed, e.g., in the SE micrographs taken after 16 h (Fig. 5e, f) or after 32 h at 1000 °C (Fig. 5g–j). Figure 6 shows a TEM analysis of ERBO/1 after 32 h at 1000 °C with precipitates of the σ - and μ -phase.

The σ -phase forms initially in the $\{111\}$ γ habit planes as can be observed in Fig. 5e or more clearly in Fig. 5i. The formation of the σ -phase is accompanied by a local enrichment of Cr and Mo in the γ -matrix at the interdendritic areas, as measured by TEM (Table 6). At 1100 °C the σ -phase seems to be not stable: precipitates were found only after short heat treatments while they disappeared after 50 h annealing time. At 1200 °C, we find no precipitates of the σ -phase at all, regardless of the annealing time.

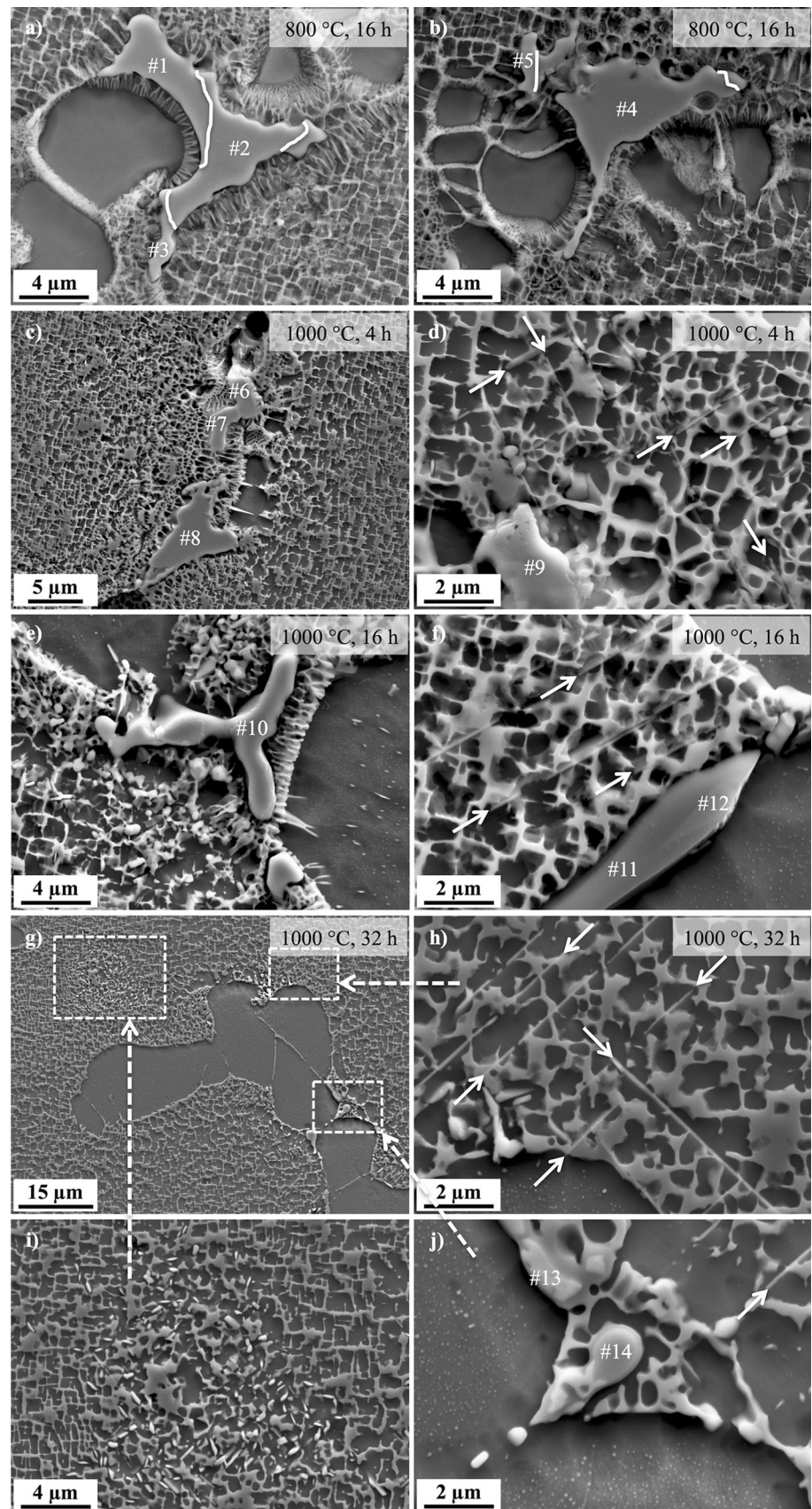
Figure 4 shows that the heating rate to 1200 °C in the solution annealing heat treatment is sufficiently fast to avoid the precipitation of the σ -phase. A short annealing time at 1200 °C or above, leads to a complete dissolution of the intermetallic Laves and μ -phase precipitates.

The chemical compositions of the precipitates as measured by EDS are compiled in Table 7 and compared to the structure map in Fig. 2d at the respective values of \bar{N} and $\Delta V/\bar{V}$. A group of precipitates identified as Laves-phase is located inside its corresponding stability region of the structure map. In addition, there are several measured particles with compositions that correspond to structure map positions slightly outside the boundaries of the Laves-phase stability region. Particles identified as μ -phase are situated inside the μ -phase stability region. The μ -phase stability region overlaps with the region of Laves stability in the structure map. For this reason, the observation of both phases during heat treatment (Fig. 4) can be rationalized by coexistence at very similar chemical composition.

Our thermodynamic calculations (Table 5), are in good agreement with the observation that annealing times longer than 8 h at 1200 °C lead to the dissolution of intermetallic precipitates, remaining only the γ/γ' -phases. In addition, for the longest heat treatment at 1100 °C, we found small amounts of the Laves/ μ -phase but no σ -phase precipitates. The heat treatments at temperatures between 800 and 1000 °C were probably too short (50 h) to reach thermodynamic equilibrium.

Another factor that can influence the thermal stability of the TCP phases is the heat treatment condition. During solution annealing the TCP phases formed in the solidification process are dissolved and the partitioning coefficients of the different elements between dendritic and interdendritic regions get closer to 1. Therefore, the tendency to form TCP phases from the as-cast condition should be higher, since there are pre-existing TCP phases and additionally elements like Re, W, Ti, and Ta are strong segregated [35], making more favorable the precipitation and growth of intermetallic phases. According to previous works on long-term aging of conventional heat-treated CMSX-4 [36], μ is the single intermetallic phase which is formed, where the precipitation of this phase at 1100 °C

Fig. 5 SEM (SE) micrographs showing intermetallic precipitates in the interdendritic areas after different heat treatments of ERBO/1. **a**, **b** 800 °C, 16 h; **c**, **d** 1000 °C, 4 h; **e**, **f** 1000 °C, 16 h; **g**–**j** 1000 °C, 32 h. White lines mark different areas found on the individual particles. White, solid line arrows indicate thin needles of the σ -phase. The numbering refers to the chemical composition measured by the SEM EDS (Table 7)



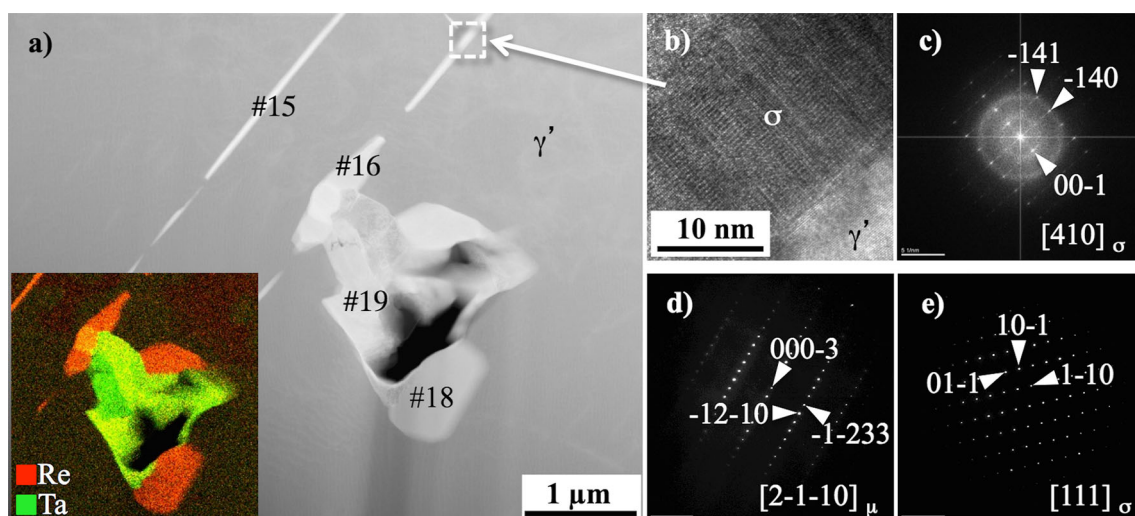


Fig. 6 TEM analysis of precipitations in ERBO/1 after 1000 °C, 32 h heat treatment. **a** STEM HAADF micrograph with an EDS inset showing the distributions of Re and Ta; **b** HRTEM micrograph of the needle-like σ -phase precipitate and **c** corresponding FFT; **d** and

e characteristic SAD patterns taken from σ and μ -phase, respectively. The numbering refers to the chemical composition measured by TEM EDS (Table 7)

Table 7 Measured chemical composition [in at.%] of intermetallic precipitates found after heat treatments (Figs. 9, 10, 11, and 12) obtained via SEM/EDX analysis. The corresponding structure map coordinates (\bar{N} , $\Delta V/\bar{V}$) according to Eqs. 1 and 2 are given in the last two columns

Precipitate number	Fraction of alloying element (at.%)											Structure map	
	Ni	Co	Cr	W	Re	Al	Ti	Ta	Mo	Hf	Phase	\bar{N}	$\Delta V/\bar{V}$
#1 (Fig. 5a)	62.7	9.9	2.8	0.2	0	3.2	1.0	2.4	0	17.9	Laves/no TCP	8.49	0.240
#2 (Fig. 5a)	21.1	12.8	39.9	7.6	7.5	2.5	0.5	0.9	6.2	1.0	μ /laves	7.34	0.149
#3 (Fig. 5a)	58.5	10.2	6.5	16.2	0.6	3.3	1.1	2.6	0.6	16.2	Laves	7.75	0.272
#4 (Fig. 5b)	62.9	9.4	2.8	0.2	0	3.6	1.0	2.3	0	17.9	Laves/no TCP	8.50	0.241
#5 (Fig. 5b)	27.8	14.2	24.3	9.9	7.7	4.7	0.9	3.5	6.0	1.0	μ /laves	7.68	0.180
#6 (Fig. 5c)	7.8	3.8	2.8	0.4	0.3	2.5	14.3	3.7	19.8	44.7	Laves	5.28	0.252
#7 (Fig. 5c)	21.0	14.6	24.2	14.5	11.5	3.4	0.6	3.7	5.8	0.7	μ /laves	7.43	0.183
#8 (Fig. 5c)	65.2	8.9	2.0	0.1	0	2.1	1.0	2.0	0	18.6	Laves/no TCP	8.53	0.237
#9 (Fig. 5d)	17.2	12.8	18.1	10.0	7.1	2.7	2.6	2.7	10.8	15.9	Laves	6.83	0.270
#10 (Fig. 5e)	20.0	16.5	46.5	5.2	4.1	1.6	0.5	0.2	5.4	0.1	Laves	7.37	0.115
#11 (Fig. 5f)	11.3	2.7	3.3	0.1	0	2.3	61.8	10.2	0.2	8.2	Laves	5.10	0.168
#12 (Fig. 5f)	7.6	0.5	1.6	0	0	2.6	56.7	8.5	0	22.6	Laves	4.72	0.163
#13 (Fig. 5j)	19.5	6.3	8.1	0.2	0	3.9	1.8	28.1	0.4	31.8	Laves	6.13	0.304
#14 (Fig. 5j)	20.3	14.9	40.7	5.4	7.1	1.6	0.5	4.0	4.8	0.8	μ /laves	7.31	0.149
#15 (Fig. 6a)	15.0	15.2	38.6	10.2	14.5	0.0	0.1	0.9	5.5	0.1	σ	7.18	0.145
#16 (Fig. 6a)	17.3	16.3	44.8	6.1	7.7	0.4	0.2	0.5	5.9	0.2	σ	7.28	0.145
#17 (Fig. 6a)	17.2	17.0	45.7	6.2	7.4	0.0	0.2	0.5	5.6	0.2	σ	7.26	0.123
#18 (Fig. 6a)	16.9	16.6	44.6	6.9	7.6	0.0	0.1	0.6	6.4	0.1	σ	7.25	0.124
#19 (Fig. 6a)	5.5	2.1	1.1	0.1	0.0	0.0	14.4	15.0	9.3	52.6	μ	4.79	0.203

starts at 10 h, according to the TTT diagram. In contrast, in our work not only μ but also σ and Laves were identified in the same time and temperature ranges.

In addition, investigations in superalloy RR2071 after conventional heat treatment and long-term exposure [7, 37], show the formation of P , μ , σ , and R phases at

temperatures below 1150 °C, where σ preferentially precipitates in the dendrite cores, and in general the density of the TCP precipitation decreases in the interdendritic areas. Other works on with CMSX-10 [38] show the formation of Re-rich TCP phases in the dendrite cores. The alloy RR2071 has a composition similar to that of CMSX-4 but

higher Mo content, and the CMSX-10 has a higher Re content. Re and Mo are a strong σ -phase former, and therefore it can be expected that the TCP precipitation is stronger in the dendrite cores. In contrast, in our work, the TCP phases are formed preferentially in the interdendritic areas. The ERBO/1 alloy has 3 wt% of Re, almost no Mo and significantly higher amount of Co (10 wt%, 3 times more than the CMSX-10). In summary, the alloy chemistry and the heat treatment state influence the element partitioning, the driving force for the precipitation of the TCP phases, and therefore their thermal stability and the location of the precipitation.

Conclusions

The microstructural stability of the ERBO/1A after during isothermal heat treatments carried out at 800, 900, 1000, 1100, and 1200 °C, with annealing times of 2, 4, 8, 16, 32, and 50 h have been characterized by electron microscopy and thermodynamic calculations based on the Calphad method. The following conclusions can be drawn from this work:

- As-cast ERBO/1A shows small amounts of μ - and Laves- phases in the interdendritic regions of the γ/γ' microstructure. These precipitates are generated due to the strong segregation of certain elements as Al, Ta, Ti, and Hf to the interdendritic areas.
- Heat treatment at 1000 °C results in formation of needle-shape σ -phase precipitates.
- Heat treatment at 1200 °C dissolves the Laves, μ -, and σ -phase.
- According to the structure map analysis the observed precipitates exhibit crystal structures that in most of the cases correspond to thermodynamic equilibrium for the respective local chemical compositions. The experimentally observed coexistence of μ - and Laves-phases can be attributed to overlapping stability regions in the structure map.
- The TTNi7 thermodynamic database does not predict the presence of all observed intermetallic phases under as-cast (Scheil–Gulliver) and isothermal treatments (equilibrium) but help to interpret the experimental results.

Acknowledgements We acknowledge financial support by the DFG through projects A3, B4, and C1 of the collaborative research center SFB/TR 103. JK, TH, and RD acknowledge financial support through ThyssenKrupp AG, Bayer Material Science AG, Salzgitter Mannesmann Forschung GmbH, Robert Bosch GmbH, Benteler Stahl/Rohr GmbH, Bayer Technology Services GmbH, the state of North-Rhine Westphalia, the European Commission in the framework of the ERDF.

Compliance with ethical standards

Conflict of Interest The authors declare that they have no conflict of interest.

References

1. Brookes CR (1982) Heat treatment, structure and properties of nonferrous alloys. ASM-International, Metals Park, OH
2. Sims CT, Stoloff NS, Hagel WC (1987) Superalloys II. Wiley, New York
3. Mao J, Chang KM, Yang W, Ray K, Vaze SP, Furrer DU (2001) Cooling precipitation and strengthening study in powder metal-lurgy U720LI. Metal Trans A 32A:2441–2452
4. Versnyder FL, Shank ME (1970) The development of columnar grain and single crystal high temperature materials through directional solidification. Mater Sci Eng 6:213–247
5. Meetham GW (1983) The development of gas turbine materials. Appl Sci Publ, London
6. McLean M (1983) Directionally solidified materials for high temperature service. The Metals Society, London
7. Lacaze J, Hazotte A (1990) Textures Microstruct. 13:1
8. Durand-Charre M (1997) The microstructure of superalloys. CRC Press, Boca Raton, FL
9. Reed R (2008) The superalloys: fundamentals and applications. Cambridge University Press, Cambridge, MA
10. Bürgel R, Maier HJ, Niendorf T (2011) Handbuch Hochtemperatur-Werkstofftechnik. Vieweg + Teubner Verlag, Wiesbaden, Germany
11. Walston S, Cetel A, MacKay R, O'Hara K, Duhl D, Dreshfield R (2004) Joint Development of a Fourth Generation Single Crystal Superalloy. In: Green KA, Pollock TM, Harada H (eds) Superalloys. TMS, Warrendale, PA, pp 15–24
12. Parsa AB, Wollgramm P, Buck H, Somsen Ch, Kostka A, Povstugar I, Choi P, Raabe D, Dlouhy A, Müller J, Spiecker E, Demtröder K, Schreuer J, Neuking K, Eggeler G (2015) Advanced scale bridging microstructure analysis of single crystal Ni-base superalloys. Adv Eng Mater 17:216–230
13. Pessah-Simonetti M, Caron P (1993) Effect of a long-term prior aging on the tensile behaviour of a high-performance single crystal superalloy. J Phys IV 03:347–350
14. Le Graverend, JB, Cormier J, Kruch S, Gallerneau F, Mendez J (2013) A strain rate sensitive formulation to account for the effect of γ' rafting on the high temperature mechanical properties of Ni-based single crystal superalloys. In: Altenbach H, Serge Kruch S (eds), Advanced materials modelling for structures. Springer, Berlin, pp 189–199
15. Yeh AC, Sato A, Kobayashi T, Harada H (2008) On the creep and phase stability of advanced Ni-base single crystal superalloys. Mater Sci Eng A 490:445–451
16. Yeh AC, Tin S (2006) Effects of Ru on the high-temperature phase stability of Ni-base single-crystal superalloys. Metall Mater Trans A 37:2621–2631
17. Pollock TM, Tin S, Martin P (2006) Nickel-based superalloys for advanced turbine engines: chemistry, microstructure and properties. J Propul Power 22:361–374
18. Pessah M, Caron P, Khan T (1992) Effect of μ phase on the mechanical properties of a nickel-base single crystal superalloy. In: Antolovich S (ed) Superalloys. TMS, Warrendale, PA, pp 567–576
19. Matuszewski K, Rettig R, Rasinski M, Kurzydowski KJ, Singer RF (2014) The three-dimensional morphology of topologically close packed phases in a high rhenium containing nickel based superalloy. Adv Mater Eng 16:171–175

20. Matuszewski K, Rettig R, Matysiak H, Peng Z, Povstugar I, Choi P, Müller J, Raabe D, Spicker E, Kurzydowski KJ, Singer RF (2015) Effect of ruthenium on the precipitation of topologically close packed phases in Ni-based superalloys of 3rd and 4th generation. *Acta Mater* 95:274–283
21. Sinha AK (1972) Topologically close-packed structures of transition metal alloys. *Prog Mater Sci* 15:79–181
22. Warren PJ, Cerezo A, Smith GDW (1998) An atom probe study of the distribution of rhenium in a nickel-based superalloy. *Mater Sci Eng A* 250:88–92
23. Darolia R, Lahrman DF, Field RD (1988) Formation of topologically closed packed phases in nickel base single crystal superalloys. In: Duhl DN, Maurer G, Antolovich S, Lund C (eds) Reichman S. *Superalloys, TMS*, pp 255–264
24. Rae C, Reed R (2001) The precipitation of topologically closed-packed phases in rhenium-containing superalloys. *Acta Mater* 49:4113–4125
25. Durand-Charre M (1997) *The microstructure of superalloys*. CRC Press, Boca Raton, FL
26. Bouse GK (1996) Eta (η) and platelet phases in investment cast superalloys. In: Kissinger RD et al (eds) *Superalloys*. TMS, Warrendale, PA, pp 163–172
27. Seiser B, Drautz R, Pettifor D (2011) TCP phase predictions in Ni-based superalloys: structure maps revisited. *Acta Mater* 59:749–763
28. Boettinger WJ, Kattner UR, Moon KW, Perepezko J (2006) NIST recommended practice guide: DTA and heat-flux DSC measurements of alloy melting and freezing, national institute of standards and technology. *Spec Publ* 960–15:1–50
29. Lukas H, Fries S, Sundman B (2007) *Computational thermodynamics: the CALPHAD method*. Cambridge University, Cambridge, MA
30. Spencer P (2008) A brief history CALPHAD. *CALPHAD* 32:1–8
31. Andersson J, Helander T, Höglund L, Shi P, Sundman B (2002) Thermo-Calc and DICTRA, computational tools for materials science. *CALPHAD* 26:273–312
32. Thermotech.co.uk and Thermo-Calc Software TTNi7 Ni-based superalloys Database Version 7, Thermo-Calc Software AB
33. Seiser B, Hammerschmidt T, Kolmogorov AN, Drautz R, Pettifor DG (2011) Theory of structural trends within 4d and 5d transition metals topologically close-packed phases. *Phys Rev B* 83:224116
34. Hammerschmidt T, Bialon AF, Pettifor DG, Drautz R (2013) Topologically close-packed phases in binary transition-metal compounds: matching high-throughput ab initio calculations to an empirical structure-map. *New J Phys* 15:115016
35. Koßmann J, Zenk CH, Lopez-Galilea I, Neumeier S, Kostka A, Huth S, Theisen W, Göken M, Drautz R, Hammerschmidt T (2015) Microsegregation and precipitates of an as-cast Co-based superalloy—microstructural characterization and phase stability modelling. *J Mater Sci* 50:6329–6338. doi:[10.1007/s10853-015-9177-8](https://doi.org/10.1007/s10853-015-9177-8)
36. Cheng KY, Jo CY, Jin T, Hu ZQ (2012) Effect of Re on the precipitation behavior of μ phase in several single crystal superalloys. *J Alloys Compd* 536:7–9
37. Rae CMF, Karunaratne MSA, Small CJ, Broomfield RW, Jones CN, Reed RC (2000) Topologically close packed phases in an experimental rhenium-containing single crystal superalloy. In: Pollock TM, Kissinger RD, Bowman RR, Green KA, McLean M, Olson S, Schirra JJ (eds) *Superalloys*. TMS, Warrendale, PA, pp 767–776
38. Acharya MV, Fuchs GE (2004) The effect of long-term thermal exposures on the microstructure and properties of CMSX-10 single crystal Ni-base superalloys. *Mater Sci Eng A* 381:143–153